Effect of oblique magnetic field on dynamic nuclear polarization in single self-assembled quantum dots governed by nuclear quadrupole interaction

Sota Yamamoto Reina Kaji Hirotaka Sasakura Satoru Adachi*

Dr. S. Yamamoto
Department of Materials Science, Tohoku University, Sendai, Japan
Prof. R. Kaji,
Prof. H. Sasakura,
Prof. S. Adachi
Division of Applied Physics, Hokkaido University, Sapporo, Japan
Email Address: sota.yamamoto.a7@tohoku.ac.jp

Keywords: *quantum dot, nuclear quadrupole interaction, nuclear spin polarization*

The dynamic nuclear spin polarization dominated by the nuclear quadrupole interaction has been studied in a single self-assembled quantum dot. Spin transfer from an optically injected spin-polarized electron to the lattice nuclear spin ensemble resulted in the nuclear spin polarization, which was probed by standard magneto-photoluminescence measurements under off-resonant excitation. In an oblique magnetic field configuration, the observed electron spin depolarization curve, the Hanle curve, had a significantly different behavior compared to the previously reported anomalous Hanle curves obtained in a transverse magnetic field. In particular, an asymmetry in the Hanle curve depending on the sign of the external magnetic field indicated that the inclination of the magnetic field largely modified the spin configurations during the dynamic nuclear spin polarization process. Numerical simulations based on a model in which the electron and nuclear spin states are described by the Bloch equation and the rate equation for the occupancy of nuclear spin eigenstates, respectively, reproduced the observations. This comparison supports the importance of the in-plane component of the principal axis of the nuclear quadrupole interaction in generating the large in-plane nuclear field, known as the anomalous Hanle effect.

1 Introduction

In semiconductor quantum dots (QDs), three dimensional strong confinement of electron wavefunction results in the enhancement of hyperfine interaction which connects an electron spin and nuclear spin ensemble [1, 2]. The hyperfine-interaction-mediated spin coupling enables to polarize the nuclear spin ensemble by optically injected spin-polarized electron. This makes QDs a promising candidate for a platform of quantum information processing such as nuclear spin memory [3–5].

For realizing these applications, it is important to understand the dynamics of the spin-coupled system in a QD. Especially, nuclear quadrupole interaction (NQI), a coupling between a nuclear spin and the electric field gradient originating from lattice strain, gets increasing the importance as a key factor for precise control of both electron and nuclear spin states [4, 6–11].

So far, we have investigated the mechanism of the anomalous Hanle effect, the generation of a large nuclear spin polarization (NSP) perpendicular to the optically injected electron spin under the influence of the NQI. The fact that the generated in-plane nuclear field is always opposite to the applied magnetic field, regardless of the sign of the electron g factor [12], suggests that the anomalous Hanle effect cannot be explained by the traditional spin cooling model [1]. Furthermore, the fact that the anomalous Hanle effect was not observed in the strain-free QD [13] suggests that the NQI induced by the residual strain in the self-assembled QD plays an important role in the realization of the anomalous Hanle effect. We proposed a dynamics model including the effect of NQI of which the main principal axes are distributed in the sample growth plane [14]. The model calculation revealed that the in-plane distribution of the principal axes is essential for the generation of in-plane nuclear field, while the out-of-plane distribution of those is required for the out-of-plane nuclear field.

In this work, for further exploration of the anomalous Hanle effect, we conducted Hanle effect measurements in self-assembled $In_{0.75}Al_{0.25}As/Al_{0.3}Ga_{0.7}As$ QDs in an oblique magnetic field. Here, the external field was inclined from the sample growth plane (xy plane), and thus the optically injected electron spin parallel to the optical axis (z axis) was not perpendicular to the magnetic field. By observing the degree

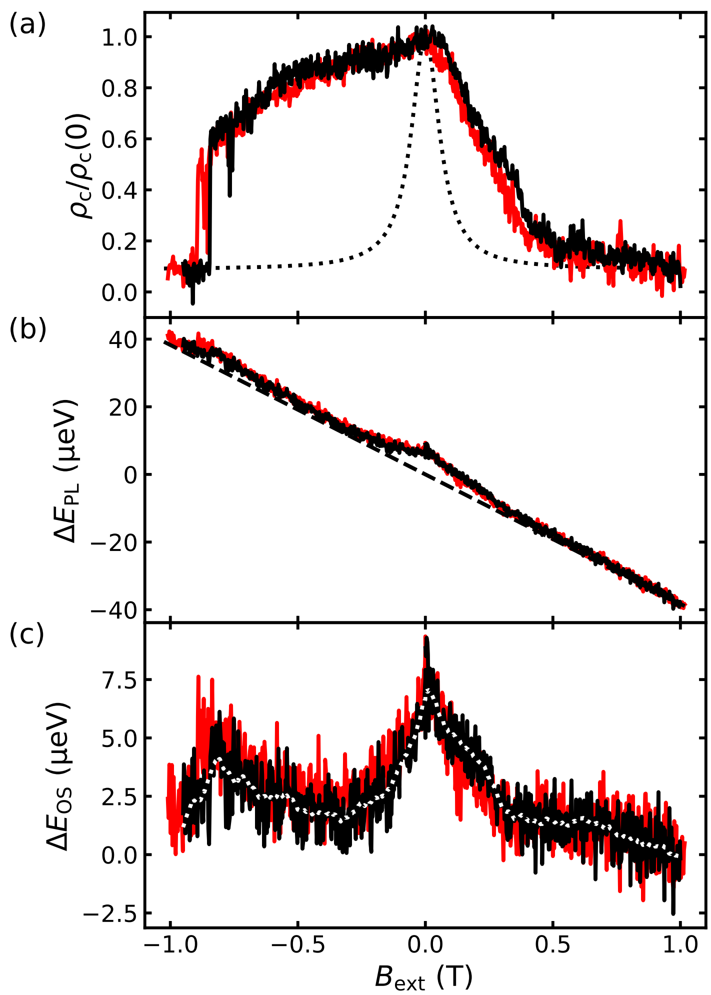

Figure 1: Results of magneto-PL measurements of positively charged exciton (X^+) in single $In_{0.75}Al_{0.25}As/Al_{0.3}Ga_{0.7}As$ self-assembled QD. Red (black) curve indicates data obtained with increasing (decreasing) magnetic field sweep. (a) Magnetic field dependence of the DCP of the X^+ PL. A dotted curve is a calculation of Hanle curve without nuclear field. The longitudinal axis is normalized by the maximum DCP, $\rho_c(0)$, which is achieved at $B_{ext} = 0$. (b) Magnetic field dependence of the energy splitting between σ^- and σ^+ polarized PLs. A dashed line is Zeeman splitting due to the external magnetic field. (c) Magnetic field dependence of the Overhauser shift obtained by subtracting the Zeeman splitting from the PL energy splitting shown in (b). The white dotted curve is a smoothed curve for guiding.

of circular polarization (DCP), ρ_c, of photoluminescence (PL) from a positively charged exciton (X^+), we probed the electron spin polarization along the z axis, $\langle S_z \rangle$. Further, from the energy splitting between σ^- and σ^+ polarized PLs, ΔE_{PL}, we analyzed the z component of the nuclear field. Comparison between the experimental observations and model calculations based on our previous model highlights the importance of the in-plane component of the main principal axis of the NQI in the generation of in-plane nuclear field.

2 Results and Discussion

Figure 1 summarizes the analysis of the Hanle effect measurements under the σ^--polarized excitation in the oblique magnetic field up to $\sim$ 1 T in magnitude. The DCP shown in Figure 1(a) decreased with increasing the magnetic field. However, the field dependence of ρ_c was different from the Hanle curve without NSP (dotted curve), of which the half-width of ~130 mT is determined by the electron g factor of 0.35 [15] and the spin lifetime of ~0.5 ns [16, 17]. In particular, the observed ρ_c in the magnetic field range of -0.8 T to 0.5 T was larger than that expected from the standard theory. This means that the optically generated NSP affected as an effective magnetic field on the electron spin: the large ρ_c pro-

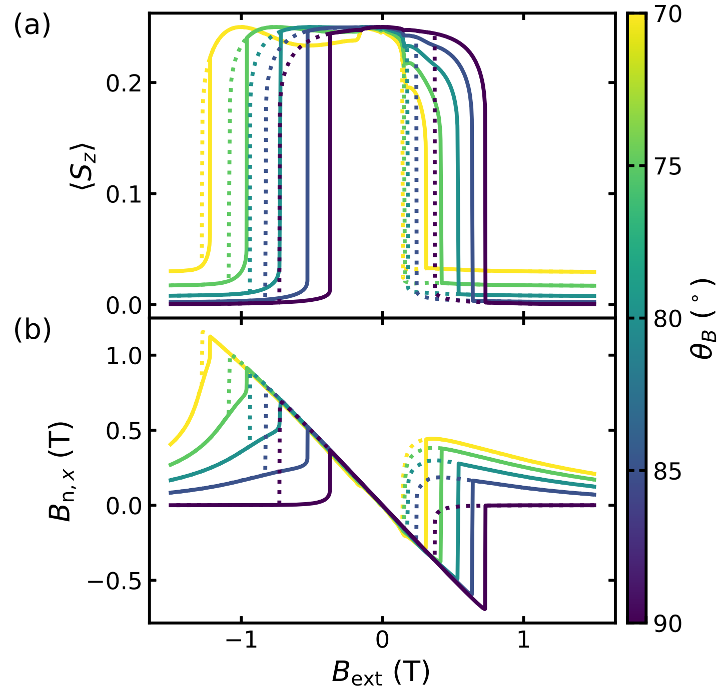

Figure 2: Results of numerical simulation assuming that all main principal axes of the NQI are in the xy plane. The color variation corresponds to the difference in the magnetic field angle, θ_B, from the z axis , indicated by the colorbar in the right side. Solid (dotted) curves are results with increasing (decreasing) magnetic field. (a) Magnetic field dependence of $\langle S_z \rangle$. (b) Magnetic field dependence of $B_{\mathrm{n},x}$.

portional to $\langle S_z \rangle$ indicates the suppression of electron spin precession owing to compensation of the external magnetic field, B_{ext}, by the nuclear field. Different from the previously reported anomalous Hanle curves [14, 15, 18], the B_{ext}-dependence of ρ_{c} was strongly asymmetric to the sign inversion of B_{ext}.
Figure 1(b) shows B_{ext}-dependence of ΔE_{PL}. This stems from the Zeeman splittings of electron and hole due to the z component of $\boldsymbol{B}_{\mathrm{ext}}$, B_z, and the Overhauser shift, ΔE_{OS}, due to the z component of nuclear field, $B_{\mathrm{n},z}$, originating from the NSP. In the figure, the Zeeman splitting due to the external field, which is proportional to B_{ext} is indicated by a dashed line. We estimated the angle between the z axis and $\boldsymbol{B}_{\mathrm{ext}}$, θ_B, as 72.8° from the fitting (see Experimental section for details).
By extracting the Zeeman splitting due to the external field, we obtained the B_{ext}-dependence of ΔE_{OS} as shown in Figure 1(c). Compared to ρ_{c}, a large asymmetry was not observed in our spectral resolution. Rather, the behavior of ΔE_{OS} was similar to that observed previously in the exact Voigt configuration, that is $\theta_B = 90°$: ΔE_{OS} decreased gradually by increasing B_{ext} and converged to zero although a magnetic field range where the ΔE_{OS} kept nonzero value was quite larger than that explained by the spin cooling model [1].

In order to understand the experimental observation, we executed simulations based on the previously proposed dynamics model [14]. **Figure 2** summarizes the results of the numerical simulations. Here it is important to note that all main principal axes of the NQI are assumed in the xy plane. It has been confirmed in Ref. 14 that this assumption is essential to explain the anomalous Hanle effect in which a large in-plane nuclear field is generated in the opposite direction to the external field. In the figure, the color variation indicates the difference in θ_B varying from 90° to 70° in 5° step. Here, $\theta_B = 90°$ corresponds to the exact Voigt configuration, and $B_z \geq 0$ is held in the region where $B_{\mathrm{ext}} \geq 0$. This is the same case as the experimental results shown in Figure 1.
Figure 2(a) shows the calculated $\langle S_z \rangle$ which was probed by ρ_{c} in the experiments as shown in Figure 1(a). While symmetric behavior in $\langle S_z \rangle$ regarding with the sign of B_{ext} appears with $\theta_B = 90°$, the asymmetric behavior is reproduced with $\theta_B \neq 90°$. In the asymmetric cases, the magnetic field region where the large $\langle S_z \rangle$ is maintained shrinks in $B_{\mathrm{ext}} > 0$ while it extends in $B_{\mathrm{ext}} < 0$. It is therefore the weight of anomalous Hanle curve seems to shift to the negative B_{ext}. This behavior is consistent with the exper-

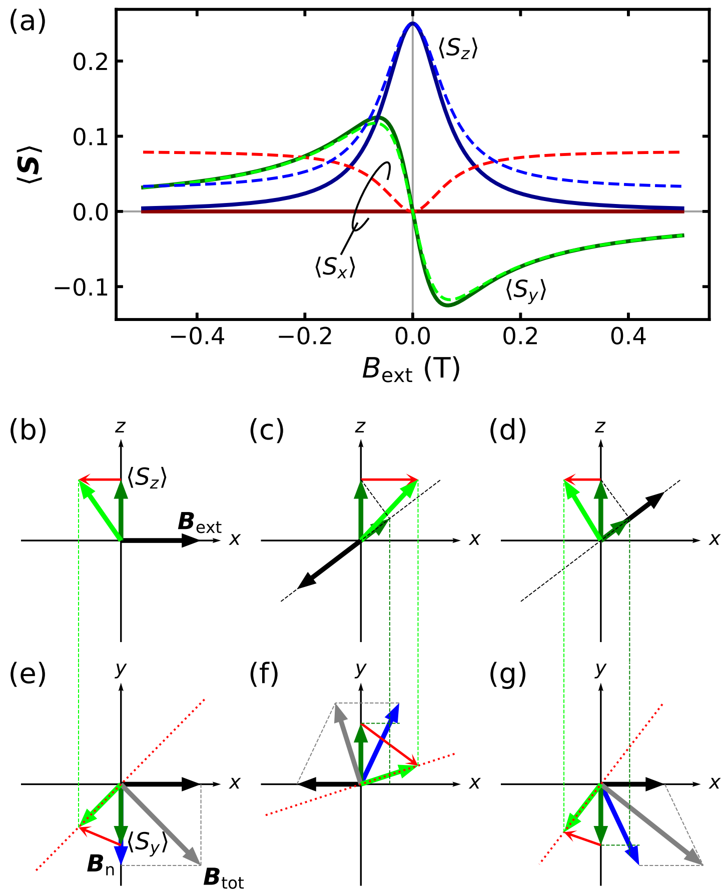

Figure 3: Interpretation of the asymmetric generation of the in-plane nuclear field using vector diagrams. (a) The steady-state electron spin polarization under magnetic field. Red, green, and blue curves are x, y, and z component of the electron spin polarization, respectively. Solid and dashed curves are calculated with the magnetic field with $\theta_B = 90°$ and $70°$, respectively. (b)–(g) The vector diagrams indicating configurations of the external field, $\boldsymbol{B}_{\mathrm{ext}}$ (black arrows), the electron spin polarization, $\langle \boldsymbol{S} \rangle$ (green and light green arrows), and the nuclear field, $\boldsymbol{B}_{\mathrm{n}}$ (blue arrows). The grey arrows indicate the total magnetic field, $\boldsymbol{B}_{\mathrm{tot}}$, given by the sum of $\boldsymbol{B}_{\mathrm{ext}}$ and $\boldsymbol{B}_{\mathrm{n}}$. The green arrows indicate $\langle \boldsymbol{S} \rangle$ without $\boldsymbol{B}_{\mathrm{n}}$, which corresponds to the configuration just after starting electron spin injection. On the other hand, the light green arrows indicate $\langle \boldsymbol{S} \rangle$ with $\boldsymbol{B}_{\mathrm{n}}$. The thin red arrows are guide for transitions of $\langle \boldsymbol{S} \rangle$. (b)–(d) and (e)–(g) are projections of respective vectors on the zx and xy plane, respectively. (b) and (e) indicate the situations under the exact Voigt geometry ($\theta_B = 90°$), while (c), (d), (f), and (g) indicate the situations under oblique magnetic field ($\theta_B > 0$) where the external field in (c) and (f) [(d) and (g)] points to the third (first) quadrant of the zx plane.

imental observation where the large ρ_{c} was maintained until B_{ext} reached about -1 T in the negative field while ρ_{c} converged to the minimum value around 0.5 T in the positive field.
The asymmetry in the calculated $\langle S_z \rangle$ reflects the behavior of in-plane nuclear field, $B_{\mathrm{n},x}$, shown in Figure 2(b), which can compensate for the external magnetic field. Since the total magnetic field on the electron spin is a sum of the external and nuclear fields, the large $\langle S_z \rangle$ is maintained when the nuclear field is opposite to the external field. This is because the electron spin precession is suppressed through the reduction of the total magnetic field. As shown in the figure, the in-plane nuclear field, which is generated symmetrically when $\theta_B = 90°$, is maintained over a broader range in the negative field than in the positive field when $\theta_B \neq 90°$. Consequently, a larger external field can be canceled out in the negative field, thereby enabling realization of the large value of $\langle S_z \rangle$ over a wide range of the negative magnetic field.

Using vector diagrams shown in **Figure 3**, the asymmetric generation of in-plane nuclear field can be interpreted as follows. In the steady state, the electron spin polarization is given by:

$$\langle \boldsymbol{S} \rangle = \frac{B_{1/2}^2 \boldsymbol{S}_0 + B_{1/2}(\boldsymbol{B}_{\rm tot} \times \boldsymbol{S}_0) + (\boldsymbol{B}_{\rm tot} \cdot \boldsymbol{S}_0)\boldsymbol{B}_{\rm tot}}{B_{1/2}^2 + B_{\rm tot}^2}. \quad (1)$$

$B_{1/2}$ is a reduced electron spin lifetime, $\tau_{\rm s}$, defined as $B_{1/2} = \hbar/(\mathrm{g_e}\mu_{\rm B}\tau_{\rm s})$. Here, $\hbar$ is the Planck constant over 2π, $\mu_{\rm B}$ is the Bohr magneton, and $\mathrm{g_e}$ is electron g factor, $\boldsymbol{S}_0$ is the maximum electron spin polarization determined by the balance of recombination and spin relaxation processes, and $\boldsymbol{B}_{\rm tot}$ is the total effective magnetic field on the electron spin given by the sum of the external field and the nuclear field, $\boldsymbol{B}_{\rm n}$, respectively. Figure 3(a) shows the calculated examples of the steady-state $\langle \boldsymbol{S} \rangle$ as a functions of $\boldsymbol{B}_{\rm ext}$, where the nuclear field is not considered. In this figure, the solid and dashed curves are the results with $\theta_B = 90°$ and $70°$, respectively.

In the exact Voigt configuration, the scenario for the buildup of in-plane nuclear field reproduced by our model is as follows. In general, the period of electron spin precession under the transverse magnetic field without nuclear field is shorter than the recombination time, and thus, $\langle S_z \rangle$ gets decreased due to the averaging. However, as shown in Figure 3(a), the y component of $\langle \boldsymbol{S} \rangle$, $\langle S_y \rangle$, is remained even in the large magnetic field where $\langle S_z \rangle$ vanishes. This is also confirmed from **Equation 1**: the first and third terms of numerator of the right hand side have no contribution to $\langle S_y \rangle$ since these are zero. On the other hand, the second term of it has a finite contribution since the finite $\tau_{\rm s}$ results in $B_{1/2} \neq 0$. This resident y component leads dynamic nuclear polarization along the y direction resulting in the deviation of $\boldsymbol{B}_{\rm tot}$, namely the spin precession axis, into the fourth quadrant of the xy plane [Figure 3(e)]. Consequently, the in-plane component of $\langle \boldsymbol{S} \rangle$ acquires the x component, $\langle S_x \rangle$, which polarizes nuclear spins in the x direction generating nuclear field along the x axis. Since $\langle S_x \rangle$ appeared in this mechanism is opposite to the external field, the generated NSP as well as nuclear field is also opposite to the external field for the spin conservation. This situation is independent of the sign of $B_{\rm ext}$, so that the generation of the in-plane nuclear field is symmetric in the exact Voigt geometry.

In the inclined magnetic field, on the other hand, the injected electron spin has parallel component to the external magnetic field as shown in Figures 3(c) and 3(d). Since this component does not precess around the external field and have nonzero value even under a large magnetic field as shown in Figure 3(a), $\langle S_x \rangle$ can contribute to generate $B_{{\rm n},x}$.

When the external field is directed in the third quadrant of the zx plane as shown in Figures 3(c) and 3(f), namely when $B_{\rm ext}$ is negative, firstly the y component of the NSP is emerged in the positive y direction and the corresponding nuclear field makes the $\boldsymbol{B}_{\rm tot}$ rotate into the second quadrant in the xy plane. Therefore, the electron spin precession plane is also changed so that its intersection with the xy plane [the red dotted line in Figure 3(g)] appears from the first to the third quadrant through the origin in the xy plane. Consequently, the in-plane component originating from the second term of Equation 1 acquires the x component. Different from the situation in the exact Voigt geometry shown in Figures 3(b) and 3(e), since this x component is amplified by the non-precessing component. Then the larger deviation in the precession axis is achieved while generating the larger in-plane nuclear field enough to compensate the external field. It is therefore, in the negative $B_{\rm ext}$, the magnetic field range with the large $\langle S_z \rangle$ is broader than that in the exact Voigt case.

On the other hand, when the external field is directed in the first quadrant of the zx plane [Figures 3(d) and 3(g)], the firstly emerging $\langle S_y \rangle$ is directed in the negative direction as shown in Figure 3(g). Accordingly, in the xy plane, the total effective field is rotated into the fourth quadrant resulting in the second-term-originating polarization directed in the third quadrant. Therefore, the x components of the second-term-originating and the non-precessing spin components are opposite each other, and thus the total magnitude of $\langle S_x \rangle$ is smaller than that in the exact Voigt case and in the negative $B_{\rm ext}$. This means it is difficult to generate a large $B_{{\rm n},x}$ in the positive $B_{\rm ext}$, and thus the magnetic field range with the large $\langle S_z \rangle$ gets narrower than that in the exact Voigt case as well as in the negative $B_{\rm ext}$. Therefore, the electron spin depolarization curve is asymmetric when the applied magnetic field is inclined.

Note that the relative direction of nuclear field to the NSP depends on the sign of electron g factor. The above explanations successfully explains the situations in our InAlAs QD system with $\mathrm{g_e} > 0$. However,

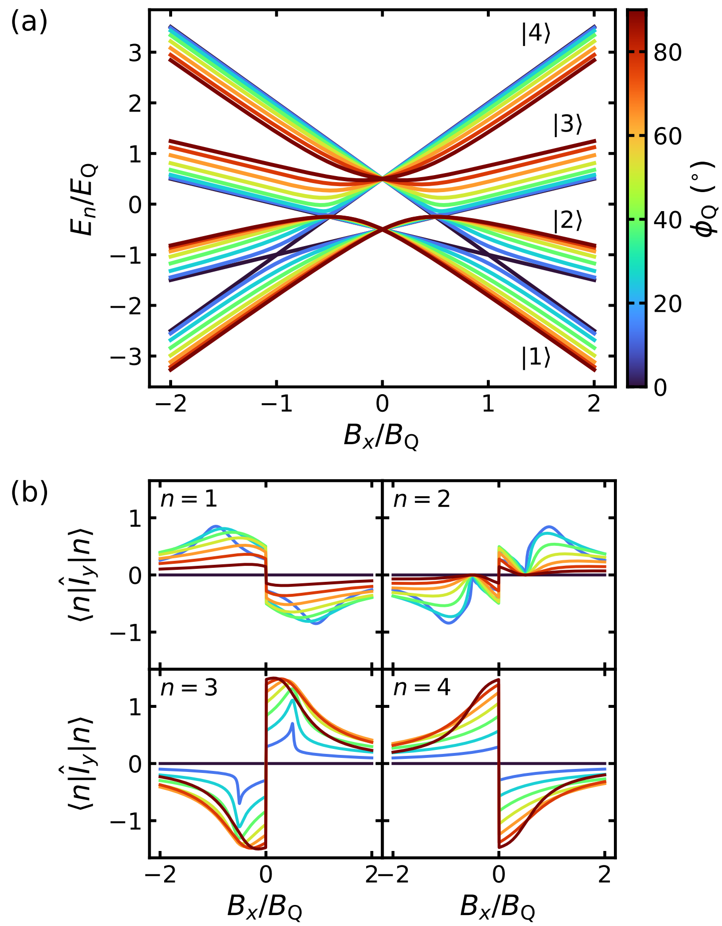

Figure 4: Nuclear spin eigenstate determined by the nuclear Zeeman and quardrupole interactions for the case of $I = 3/2$ where the magnetic field is assumed along the x axis and the main principal axis of the NQI is assumed in the xy plane. The color variation of curves reflects the difference in the azimuth angle of the main principal axis of the NQI, ϕ_Q, as indicated in the colorbar. The horizontal axis is normalized by the reduced strength of the NQI, B_Q, in terms of magnetic field. (a) Nuclear spin eigenenergy, E_n. The vertical axis is normalized by the NQI energy, E_Q. (b) Expectation value of spin operator $\hat{I}_y$ calculated for the eigenstates $|n\rangle$ ($n = 1, 2, 3, 4$) where the number n is the same as that indicated in (a). Note that the crossing of eigenstates occurs only when $B_x = 0$ for all ϕ_Q and $B_x/B_Q = \pm 1/2, \pm 1$ for $\phi_Q = 0$ in the considered configuration.

the similar scenario for $g_e < 0$ also holds true. In the latter case, $B_{1/2}$ in the Equation 1 is negative and the second-term-originating component of electron spin and the resultant NSP emerges in the opposite direction to the case of $g_e > 0$. Since nuclear field is proportional to the NSP with a factor $2A/(g_e\mu_B)$ where A is the hyperfine constant, the resultant nuclear field with $g_e < 0$ is generated in the same direction as $g_e > 0$, which can compensate for the external field.

The generation of the y component of NSP which is a key ingredient to the emergence of in-plane nuclear field opposite to the external field is guaranteed by the in-plane distribution of main principal axis of the NQI. This can be understood by considering the nuclear spin eigenstates. **Figure 4** shows the eigenstates of nuclear spin with spin $I = 3/2$ determined by the nuclear Zeeman and quadrupole interactions. Here the magnetic field is assumed to be aligned with the x axis, and the main principal axis of the NQI is assumed to be oriented in any direction within the xy plane. The difference in the azimuth angle of the principal axis, ϕ_Q, is indicated by the difference in the color. In the figure, only the results with $0° \leq \phi_Q \leq 90°$ are indicated because there is symmetry in the ϕ_Q-dependence every 90°. As shown in Figure 4(a), the spin state degeneracy at $B_x = 0$ is resolved by the NQI. Further, in the small B_x, the eigenstate is strongly dominated by the NQI: the eigenenergy, E_n, depends nonlinearly on B_x and on ϕ_Q. On the other hand, in the large B_x, the eigenenergy becomes linear to B_x regardless of ϕ_Q. This means that the eigenstate converges to the pure Zeeman eigenstate since the relative strength of the NQI to the

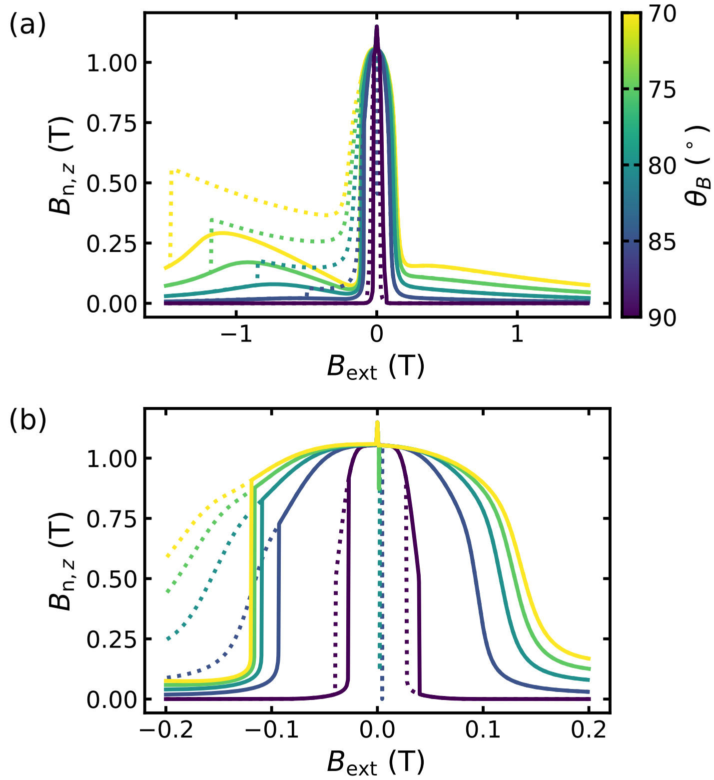

Figure 5: Magnetic field dependence of $B_{\mathrm{n},z}$ calculated by assuming that all main principal axes of the NQI are along the z axis. The color variation corresponds to the difference in the magnetic field angle from the z axis as shown in a colorbar in the right side. Solid (dotted) curves are results with increasing (decreasing) magnetic field. (b) is enlarged view of (a), which shows $B_{\mathrm{n},z}$ around $|B_{\mathrm{ext}}| \leq 0.2$ T.

Zeeman interaction decreases.
Figure 4(b) shows the expectation value of $\hat{I}_y$, which observes the spin momentum along the y axis, calculated for the nuclear eigenstates $|n\rangle$, $(n = 1, 2, 3, 4)$ where the number n corresponds to that indicated in Figure 4(a). The emergence of nonzero NSP in the y direction requires that any of the expectation values of operator $\hat{I}_y$ is not equal to zero. This is due to the fact that our model assumes that the effective NSP, $\langle I_\xi \rangle$, for $\xi = x,\ y$, and z is given by:

$$\langle I_\xi \rangle = \sum_n p_n \langle n|\hat{I}_\xi|n\rangle, \tag{2}$$

where p_n is occupancy of the eigenstate indexed by n. With this definition, a coherent correlation among nuclei in the electron confinement volume is neglected. Namely, when $\langle n|\hat{I}_y|n\rangle = 0$ for all n, no distribution can realize $\langle I_y \rangle \neq 0$. As shown in Figure 4(b), $\langle n|\hat{I}_y|n\rangle$ has nonzero value regardless of ϕ_{Q} in the magnetic field region where the NQI has significant impact on the eigenstates of nuclei except $\phi_{\mathrm{Q}} = 0$ where the main principal axis and the magnetic field are parallel. Such a nonzero $\langle n|\hat{I}_y|n\rangle$ cannot be realized when the NQI is inefficient, and when the main principal axis aligns with the z direction even if the NQI is efficient. Namely, the main principal axes of the NQI should have the component within the xy plane for generating the in-plane nuclear field. Furthermore, considering the fact that the anomalous Hanle curve was observed independent of the azimuth angle of the magnetic field [19], the distribution of the main principal axes should have cylindrical symmetry around the sample growth axis (z axis) since the $\langle n|\hat{I}_y|n\rangle$ has the ϕ_{Q}-dependent periodicity.

Finally, numerical simulations, which can be compared with the observed behaviors of $B_{\mathrm{n},z}$ are presented. By considering the effect of the z component of main principal axes of the NQI, the magnetic field dependencies of $B_{\mathrm{n},z}$ in the transverse and oblique magnetic fields are calculated as shown in **Figure 5**(a). Similar to Figure 2, the color variation indicates the difference in the angle θ_B of the external magnetic

field from the z axis. While $B_{n,z}$ in the exact Voigt configuration is symmetric with respect to the sign of B_{ext} in whole magnetic field region, the $B_{n,z}$ in the inclined external field is divided into the two regions: small and large magnetic field regions.
Figure 5(b) shows an enlarged view of the range $|B_{ext}| \leq 0.2$ T in Figure 5(a). At $B_{ext} = 0$, the calculated $B_{n,z}$ has the maximum values independent of θ_B and gradually decreases by increasing $|B_{ext}|$. Therefore, $B_{n,z}$ indicates a peak-like structure centered at around $B_{ext} = 0$. Note that the sharp dip at the magnetic field very close to $B_{ext} = 0$ with $\theta_B \neq 90°$ originates from the compensation of B_z by the z component of the Knight field, the effective magnetic field on the nuclei originating from the electron spin polarization. At this point, the z component of the total effective magnetic field on the nuclei reduces to zero which results in the reduction of the NSP [20, 21].
On the other hand, in the limit of a large magnetic field, the only remaining component of the electron spin polarization is parallel to the external field; the other components are averaged out during the fast spin precession. Therefore the situation is converged to that observed in the Faraday geometry. That is, the reproduced asymmetry in the large $|B_{ext}|$ region can be considered similarly to the phenomenon known as bistability arising from the energy conservation during the electron-nuclear spin-flip process via the hyperfine interaction [22–24].
The former characteristic is consistent with the experimentally observed ΔE_{OS} shown in Figure 1(c). Furthermore, the value of ΔE_{OS} appears to increase as B_{ext} approaches from 0.0 T to −0.8 T. This behavior is also consistent, as reproduced in Figure 5.

3 Conclusion

In a single self-assembled InAlAs QD, we studied the dynamic polarization of nuclear spins dominated by the NQI under the oblique magnetic field deviated from the sample growth plane. The Hanle curve, which probes the electron spin polarization along z axis, revealed the asymmetric generation of in-plane nuclear field with respect to the sign of magnetic field. This behavior is significantly different from the previously reported symmetric anomalous Hanle curves. By using semi-classical model based on the Bloch equation of electron spin and the rate equation for the occupancy of nuclear eigenstates, we considered the dynamics behind the observed phenomenon. The numerical simulations captured the asymmetry observed in the self-assembled QD, and it gave an interpretation about the transition from the symmetric to the asymmetric anomalous Hanle curves. The key ingredient for the generation of the large in-plane nuclear field is stabilization of the y component of the NSP, which is perpendicular to the optically injected electron spin and the external field as well as the in-plane nuclear field which compensates for the external field. Under the influence of the NQI whose main principal axes are within the xy plane, the nonzero y component of the nuclear field can be stabilized. By precessing around the y component of the nuclear field, the electron spin polarization acquires the x component that does not vanish on time average. In the exact Voigt configuration, since this x component is symmetric with respect to the sign inversion of the magnetic field, the symmetric anomalous Hanle curve is explained, as previous studies. On the other hand, in the tilted configuration used in this study, the non-precessing component of the electron spin polarization appears as an offset in the x direction. Therefore the x component of the electron spin polarization becomes asymmetric with respect to the magnetic field, and the asymmetric anomalous Hanle curve is explained. The fact that the asymmetry observed in this study can be consistently explained supports the concept of the previously proposed model. These observations and calculations further deepen the understating of the effect of NQI from the microscopic viewpoint.

4 Experimental Section

In this study, we used single self-assembled $In_{0.75}Al_{0.25}As/Al_{0.3}Ga_{0.7}As$ QD grown by molecular beam epitaxy on a (001) GaAs substrate [25]. For a large mismatch in lattice constants between the capping layer and the QD layer, the QDs have grown in the Stranski-Krastanov mode, leaving the lattice strain

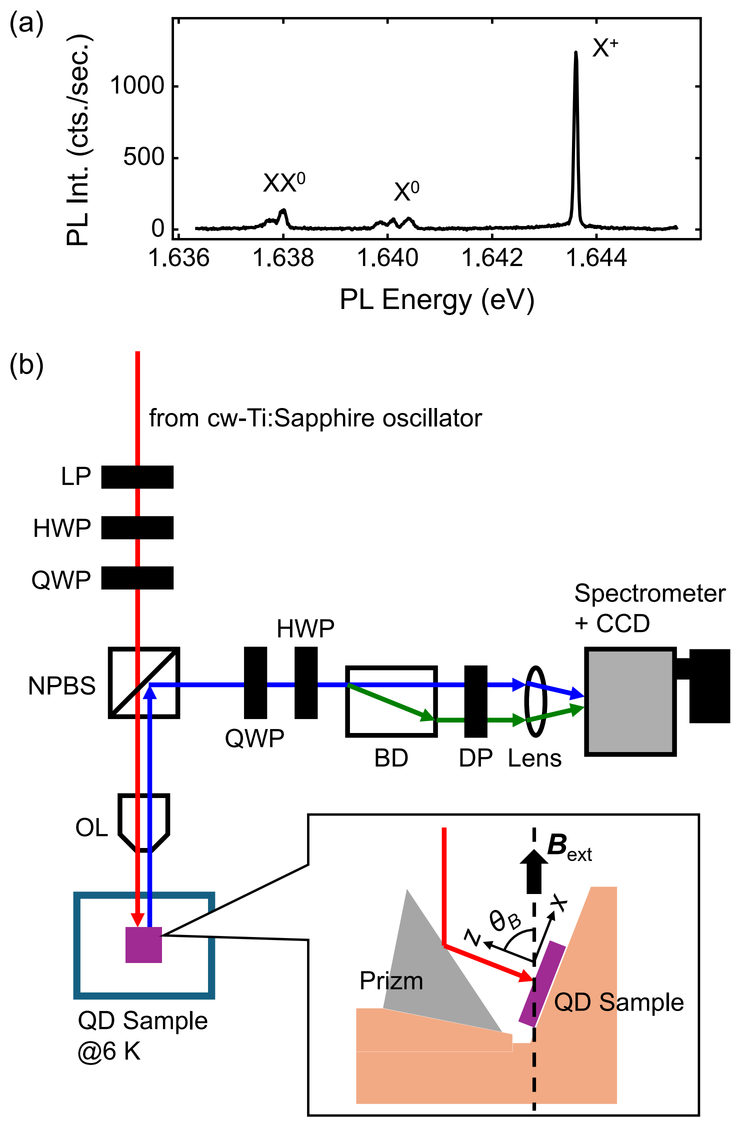

Figure 6: Experimental setup. (a) PL spectrum from the single self-assembled $In_{0.75}Al_{0.25}As/Al_{0.3}Ga_{0.7}As$ QD. (b) A schematic of the optical system utilized for the time-integrated magneto-PL measurements. The inset is a side view of the sample holder for introducing the incilined magnetic field.

inside the QD. By fabricating small mesa structures, single QD PL measurements were performed. **Figure 6**(a) shows typical PL spectra from the single QD. We focused on the PL from a positive trion state (X^+) of which the DCP is directly proportional to the electron spin polarization through the relation $\rho_c = 2\langle S_z \rangle$. Here we defined the DCP as $\rho_c = (I^- - I^+)/(I^- + I^+)$ where $I^\pm$ is the integrated intensity of the $\sigma^\pm$-polarized PL.

From the independent study, the electron g factor in our InAlAs QD was revealed to have opposite sign to the In(Ga)As QD systems [26]. Since the anomalous Hanle effect is observed in both InAlAs and In(Ga)As QDs [12, 15, 18, 27], the spin cooling model, in which the direction of the nuclear field is determined by the sign of g factor [1], cannot explain the anomalous Hanle effect. Furthermore, isotropic nature of the electron g factor was confirmed from the polarization-resolved magneto-PL measurements in the Faraday and Voigt geometries [15, 26]. Therefore, the asymmetry observed in this study is different from the phenomenon observed in GaAs quantum wells which can be explained based on the spin cooling model [28]. Some other observations regarding with the anomalous Hanle effect, such as excitation power dependence [29], the effect of excitation helicity oscillation [29], or the temporal evolution of PL polarization [14], are available in the corresponding references.

Figure 6(b) shows a schematic of optical system. A continuous-wave Ti:sapphire oscillator (Spectra Physics 3900S) supplied excitation light with wavelength of ∼730 nm corresponding to the wetting layer of the QD sample. After passing through a linear polarizer (LP), a half-wave plate (HWP), and a quarter-wave plate (QWP) in this order, the circularly polarized excitation light was focused on the sample surface by a objective lens (OL, Mitsutoyo M Plan Apo NIR x20). PL from the QD collected by the same OL was spatially separated by a combination of a QWP, a HWP, and a beam displacer (BD), dispersed by a spectrometer (Horiba JY T64000), and then detected by a liquid-nitrogen-cooled charge-coupled device (CCD, Nippon Roper Spec-10:100BR). A depolarizer (DP) in front of the spectrometer was used to resolve difference in the diffraction efficiency of the grating depending on the light polarization. Although the energy resolution of this system is $\sim 13\ \mu$eV, the effective energy resolution is improved to $\lesssim 5\ \mu$eV by spectral fitting.

The sample was kept at 6 K throughout the experiments in an optical cryostat (Oxford Instruments MicrostatBT). The external magnetic field was generated by a superconducting magnet. To tilt the magnetic field, we used a sample holder schematically shown in the inset of Figure 6(b). Since the surface on which the sample is mounted is tilted, the magnetic filed deviated from the sample growth plane can be applied. Further, a prism which leads the excitation light to the sample surface and collects the PL from the sample is installed, and its tilted angle was designed for the normal incidence to the sample. To estimate the actual magnetic field angle, θ_B, assuming that the effect of nuclear field is small in the large external field, a linear fit to $\Delta E_{\rm PL}$ in $|B_{\rm ext}| > 1$ T yielded $(\mathrm{g_e} + \mathrm{g_h})\mu_{\rm B} \cos\theta_B$. Using the electron and hole g-factors, $\mathrm{g_e}$ and $\mathrm{g_h}$, obtained from the independent measurements [26], we estimated $\theta_B = 72.8°$. Actually, this value is different from that determined by the design of the sample holder, which is $\sim 68.8°$. The difference might arise from an unintended missalignment of the apparatus such as the sample holder or cryostat, which causes additional inclination relative to the magnetic field generated by the superconducting magnet.

Our model is based on the Bloch equation of the electron spin polarization and the rate equation for p_n in Equation 2, the occupancy of the nuclear eignestates. For simplicity, in this study we treated the system contains only single nuclear species with spin quantum number of 3/2. Detailed description can be found in Ref. 14. In the calculation shown in Figure 3, we assumed that all of the main principal axes of the NQI are in the xy plane. More specifically, we assumed 32 different axes each of which is directed in the $(x, y, z) = (\cos\phi_{\mathrm{Q},j}, \sin\phi_{\mathrm{Q},j}, 0)$ where $\phi_{\mathrm{Q},j} = (2j + 1)\pi/32$ for $j = 0, \cdots, 31$. On the other hand, in Figure 5, we assumed that the main principal axis of the NQI is along the z axis. In the actual QD, intermediate situation between these two assumptions are considered to exist, however we consider that it is sufficient to assume two extreme conditions for the purposes of describing the characteristics of the NQI. It should be noted that the wide distribution of main principal axes is predicted from the computational study [30].

Acknowledgements

We acknowledge the support of Japan Society for the Promotion of Science (20K03812 and 21H01745).

References

[1] F. Meier, B. P. Zakharchenya, editors, *Optical Orientation*, volume 8 of *Modern Problems in Condensed Matter Sciences*, North-Holland, Amsterdam, **1984**.

[2] B. Urbaszek, X. Marie, T. Amand, O. Krebs, P. Voisin, P. Maletinsky, A. Högele, A. Imamoglu, *Rev. Mod. Phys.* **2013**, *85* 79.

[3] J. M. Taylor, C. M. Marcus, M. D. Lukin, *Phys. Rev. Lett.* **2003**, *90* 206803.

[4] D. A. Gangloff, G. Éthier-Majcher, C. Lang, E. V. Denning, J. H. Bodey, D. M. Jackson, E. Clarke, M. Hugues, C. Le Gall, M. Atatüre, *Science* **2019**, *364*, 6435 62.

[5] E. V. Denning, D. A. Gangloff, M. Atatüre, J. Mørk, C. Le Gall, *Phys. Rev. Lett.* **2019**, *123* 140502.

[6] C.-W. Huang, X. Hu, *Phys. Rev. B* **2010**, *81* 205304.

[7] A. Högele, M. Kroner, C. Latta, M. Claassen, I. Carusotto, C. Bulutay, A. Imamoglu, *Phys. Rev. Lett.* **2012**, *108* 197403.

[8] E. A. Chekhovich, M. Hopkinson, M. S. Skolnick, A. I. Tartakovskii, *Nature Communications* **2015**, *6*, 1 6348.

[9] R. Stockill, C. Le Gall, C. Matthiesen, L. Huthmacher, E. Clarke, M. Hugues, M. Atatüre, *Nature Communications* **2016**, *7*, 1 12745.

[10] R. Matsusaki, R. Kaji, S. Yamamoto, H. Sasakura, S. Adachi, *Applied Physics Express* **2018**, *11*, 8 085201.

[11] E. A. Chekhovich, S. F. C. da Silva, A. Rastelli, *Nature Nanotechnology* **2020**, *15*, 12 999.

[12] S. Yamamoto, R. Matsusaki, R. Kaji, S. Adachi, *Journal of Physics: Conference Series* **2019**, *1220* 012047.

[13] G. Sallen, S. Kunz, T. Amand, L. Bouet, T. Kuroda, T. Mano, D. Paget, O. Krebs, X. Marie, K. Sakoda, B. Urbaszek, *Nature Communications* **2014**, *5*, 1 3268.

[14] S. Yamamoto, R. Kaji, S. Adachi, *Phys. Rev. B* **2023**, *108* 054422.

[15] S. Yamamoto, R. Matsusaki, R. Kaji, S. Adachi, *Phys. Rev. B* **2018**, *97* 075309.

[16] H. Kumano, S. Kimura, M. Endo, H. Sasakura, S. Adachi, S. Muto, I. Suemune, *Journal of Nanoelectronics and Optoelectronics* **2006**, *1*, 1 39.

[17] R. Kaji, S. Adachi, H. Sasakura, S. Muto, *Phys. Rev. B* **2012**, *85* 155315.

[18] O. Krebs, P. Maletinsky, T. Amand, B. Urbaszek, A. Lemaître, P. Voisin, X. Marie, A. Imamoglu, *Phys. Rev. Lett.* **2010**, *104* 056603.

[19] S. Yamamoto, T. Arakawa, R. Matsusaki, R. Kaji, S. Adachi, *physica status solidi (b)* **2020**, *257*, 2 1900381.

[20] C. W. Lai, P. Maletinsky, A. Badolato, A. Imamoglu, *Phys. Rev. Lett.* **2006**, *96* 167403.

[21] M. S. Kuznetsova, K. Flisinski, I. Y. Gerlovin, I. V. Ignatiev, K. V. Kavokin, S. Y. Verbin, D. R. Yakovlev, D. Reuter, A. D. Wieck, M. Bayer, *Phys. Rev. B* **2013**, *87* 235320.

[22] P.-F. Braun, B. Urbaszek, T. Amand, X. Marie, O. Krebs, B. Eble, A. Lemaitre, P. Voisin, *Phys. Rev. B* **2006**, *74* 245306.

[23] A. I. Tartakovskii, T. Wright, A. Russell, V. I. Fal'ko, A. B. Van'kov, J. Skiba-Szymanska, I. Drouzas, R. S. Kolodka, M. S. Skolnick, P. W. Fry, A. Tahraoui, H.-Y. Liu, M. Hopkinson, *Phys. Rev. Lett.* **2007**, *98* 026806.

[24] R. Kaji, S. Adachi, H. Sasakura, S. Muto, *Phys. Rev. B* **2008**, *77* 115345.

[25] T. Yokoi, S. Adachi, H. Sasakura, S. Muto, H. Z. Song, T. Usuki, S. Hirose, *Phys. Rev. B* **2005**, *71* 041307.

[26] R. Kaji, R. Matsusaki, S. Yamamoto, S. Adachi, *Japanese Journal of Applied Physics* **2019**, *58*, SB SBBH05.

[27] J. Nilsson, L. Bouet, A. J. Bennett, T. Amand, R. M. Stevenson, I. Farrer, D. A. Ritchie, S. Kunz, X. Marie, A. J. Shields, B. Urbaszek, *Phys. Rev. B* **2013**, *88* 085306.

[28] V. Kalevich, V. Korenev, *Jetp Letters - JETP LETT-ENGL TR* **1992**, *56*.

[29] R. Kaji, S. Yamamoto, R. Matsusaki, S. Adachi, *Japanese Journal of Applied Physics* **2019**, *58*, SB SBBH10.

[30] C. Bulutay, E. A. Chekhovich, A. I. Tartakovskii, *Phys. Rev. B* **2014**, *90* 205425.